Photoacoustics 18 (2020) 100165

Contents lists available at ScienceDirect

Photoacoustics

journal homepage: www.elsevier.com/locate/pacs

Lipid-weighted intraoperative photoacoustic tomography of breast tumors: Volumetric comparison to preoperative MRI

Ivan Kosik[a,b], Muriel Brackstone[c,d], Anat Kornecki[a,e], Astrid Chamson-Reig[a], Philip Wong[a,b], Jeffrey J.L. Carson[a,b,d,f,*]

[a] Imaging Program, Lawson Health Research Institute, London, Ontario, Canada
[b] Department of Medical Biophysics, Schulich School of Medicine and Dentistry, The University of Western Ontario, London, Ontario, Canada
[c] Department of Oncology, Schulich School of Medicine & Dentistry, The University of Western Ontario, London, Ontario, Canada
[d] Department of Surgery, Schulich School of Medicine & Dentistry, The University of Western Ontario, London, Ontario, Canada
[e] Department of Medical Imaging, Schulich School of Medicine and Dentistry, The University of Western Ontario, London, Ontario, Canada
[f] Department of Physics and Astronomy, Schulich School of Medicine and Dentistry, The University of Western Ontario, London, Ontario, Canada

ARTICLE INFO

Keywords:
Photoacoustic tomography
Breast cancer
Intraoperative imaging
Lipid weighted imaging
Dynamic contrast enhanced MRI
Tumor volume
Acoustic transducers

ABSTRACT

With a lifetime risk of 1 in 8, breast cancer continues to be a major concern for women and their physicians. The optimal treatment of the disease depends on the stage of the cancer at diagnosis, which is typically assessed using medical imaging. However, currently employed imaging systems for breast tumor measurement rarely agree perfectly.

Our group developed an Intraoperative Photoacoustic Screening (iPAS) soft tissue scanner featuring high bulk tissue sensitivity, a clinically compatible scan-time of 6 min, imaging depths greater than 2 cm and the capability to visualize whole breast tumors based on their lipid, rather than hemoglobin, profile. Here, we report on the first clinical experience with breast cancer patients by comparing tumor-measurement using iPAS, preoperative dynamic contrast enhanced magnetic resonance imaging (DCE-MRI) and gold-standard pathology. Tumor size was measured volumetrically for iPAS and DCE-MRI, and separately using maximum diameters for pathology, DCE-MRI and iPAS. Comparisons were performed using Pearson's correlation coefficients, and the non-parametric Wilcoxon signed-rank test.

Twelve consecutive patients were included in the study, contingent on pathologically documented invasive carcinoma. iPAS volumetric tumor size was positively correlated to DCE-MRI (Pearson's $r = 0.78$, $p = 0.003$) and not significantly different (Wilcoxon, $p = 0.97$). In comparison to pathology, tumor diameters given by iPAS were positively correlated (Pearson's $r = 0.87$, $p = 0.0002$) and significantly different (Wilcoxon, $p = 0.0015$).

The results indicated that volumetric-measurement of invasive breast tumors with iPAS is similar to that of DCE-MRI. On the other hand, tumor diameter measurements were less reliable. Beyond enhancing surgical specimen examination, an extension of this technology to diagnostic imaging promises a new perspective on tumor assessment, potentially improving our current understanding and treatment of breast cancer.

1. Introduction

1.1. Overview

Breast cancer is among the most frequent cancers to affect women, exhibiting an average lifetime risk of 1 in 8 [1]. It is a complex disease that is of particular concern for aging women and those with family history of cancer. To combat breast cancer, and due to the availability of medical imaging technology, routine breast cancer screening is now a relatively standard practice in the developed world [2]. Most women over the age of 50, or younger at-risk individuals, are encouraged to undertake standardized annual mammograms as well as any appropriate follow-up procedures [3,4]. In cases that lead to a cancer diagnosis, medical imaging is used to evaluate, or stage, the cancer [5]. For example, due to their small size, the ideal treatment of stage I and most stage II cancers involves Breast Conserving Surgery (BCS) [6]. One of the goals of BCS is to remove the whole tumor while sparing the neighboring healthy tissue. This is often accomplished by use of various medical imaging systems which permit the surgeon to localize the suspect lesion with better accuracy than physical examination alone [7].

* Corresponding author at: Imaging Program, Lawson Health Research Institute, London, Ontario, Canada.
E-mail address: jcarson@lawsonimaging.ca (J.J.L. Carson).

https://doi.org/10.1016/j.pacs.2020.100165
Received 11 September 2019; Received in revised form 7 January 2020; Accepted 29 January 2020
Available online 24 April 2020

By monitoring neoadjuvant therapy, medical imaging continues to play a vital role in the treatment of stage III and higher breast cancers, as well as tumors which are inoperable due to location or extent [8]. The aim of neoadjuvant therapy is to reduce the cancer extent, or tumor size, and potentially down-stage the cancer. In responding patients this treatment course may open up new surgical options such as BCS versus radical mastectomy, or even facilitate a surgical option when there was none before. Indeed, the size of the tumor in primary breast cancer is the single most important factor determining the cancer stage [9]. As a result, the accuracy of tumor measurement can have a significant effect on selecting an appropriate follow-up action, as reflected in the widely adopted revised Response Evaluation Criteria in Solid Tumors (RECIST v1.1, released 2009) originally prepared by the International Working Group [10]. Amongst other changes, the updated definition of "tumor progression" now includes an absolute increase of the largest tumor diameter by a minimum of 5 mm. Compared to the previous criteria of a minimum 20 % increase in size, this new standard places a premium on medical imaging precision and accuracy, however, it also promotes better evaluation of patient response to therapy, further maximizing survival, especially for stage III and higher cancers [11].

There are many possible candidate techniques for the assessment of disease extent or tumor size. Currently, the accepted gold standard is postsurgical pathological examination. Unfortunately, for obvious reasons, the examination results are not available to guide pre-surgical decisions. Physical breast examination via palpation remains useful due to its relative simplicity, however, clinical trials have shown palpation to be one of the least accurate techniques in correlation with pathological examination [12]. Fluorine-18-Fluorodeoxyglucose Positron Emission Tomography (18FDG-PET), an excellent whole body distant metastasis detector, has been proposed and occasionally used to assess breast tumor stage and monitor therapy efficacy. However, the procedural complexity as well as use of radiotracers, combined with limited sensitivity for small ($< 2-3$ cm) tumors and rather high false positive rate, reduces the utility of PET as an efficient tumor size assessment tool [13].

As a generally accepted breast cancer screening tool and due to its relatively good balance between cost, complexity, sensitivity and specificity, X-ray mammography is perhaps the most widely used breast imaging technique [2,12]. However, studies show that this 2-D imaging modality suffers from significant sensitivity and specificity reduction in younger patients, and independently in denser breasts, particularly when monitoring response to neoadjuvant therapy [14]. Ultrasonography (US) has demonstrated better sensitivity than mammography but suffers from lesion size underestimation and, due to its operator dependence as well as 2-D nature, is not a reproducible procedure with good repeatability statistics [5,12,15]. On the other hand, dynamic contrast enhanced magnetic resonance imaging (DCE-MRI) has established itself as the best single imaging modality in the detection and evaluation of breast cancer. It's effectiveness has been validated in numerous studies and shown to be superior to both mammography and ultrasound [5,8,15]. On the downside, large studies have demonstrated specificity deficits caused by high background parenchymal enhancement as well as detection of numerous non-specific lesions. In practice, these shortcomings limit DCE-MRI to mammographically/sonographically occult lesions and cases where mammography and US produce ambiguous findings [16].

The debate about how best to perform tumor extent assessment is ongoing. However, there is broad agreement on several fronts. For example, the current standard of unidimensional tumor measurement is likely to change in the near future due to the clinically demonstrated superiority of 3-dimensional assessment. In fact, the International Working Group, while preparing the revised version of RECIST (v1.1, 2009), noted that, in regards to volumetric tumor assessment, they "*did not believe that there is at present sufficient standardization and widespread availability to recommend adoption.*" [10] This conclusion suggests that RECIST guidelines will reflect a technologically viable solution once it is available and sufficiently standardized. Beyond 3D visualization, other desirable features of such a potentially viable breast imaging solution include simplicity, low cost, operator independence and breast density independence.

Photoacoustic tomography (PAT) is a relatively new imaging modality with limited clinical experience. [17–21] Nevertheless, it has demonstrated highly desirable features, especially with respect to breast imaging [18]. For example, PAT employs tissue-safe near infrared laser illumination thereby avoiding problems associated with ionizing radiation such as in mammography. Furthermore, PAT is a relatively inexpensive and fast imaging technique, especially compared to MRI. Moreover, PAT makes use of endogenous optical contrast of blood, lipids and other soft tissues, eliminating the need for exogenous contrast agents, and hence, speeding up and simplifying the imaging protocol [22,23]. Because the basis of PAT is an intrinsically 3D phenomenon, called the photoacoustic effect, it is easily implemented as a 3D imaging modality, eliminating the concern for operator dependence. [18,24,25] And finally, PAT imaging has been shown to be breast density independent, as opposed to mammography and US which derive contrast based on tissue density [19].

In biomedical applications, photoacoustic tomography usually employs a pulsed laser to illuminate the tissue of interest. After illumination, wavelength-targeted chromophores inside the tissue, typically oxy or deoxy hemoglobin, preferentially absorb the light energy and undergo a process known as the photoacoustic effect. The result is the generation and emission of a transient acoustic pressure wave, which travels in all directions away from its origin. An acoustic transducer, or array of transducers surrounding the tissue, can then be used to measure the time-resolved properties of the pressure wave, which in turn informs about the size, location, and optical properties of the absorber. By combining many such measurements, in conjunction with an image reconstruction technique such as back-projection, a 3-dimensional map of the concentration of the relevant chromophores can be generated.

To date, most breast cancer PAT imaging studies targeted cancer-induced angiogenesis via hemoglobin as the primary indicator of malignancy. Moreover, only a few studies utilizing multispectral PAT for lumpectomy margin assessment have been carried out [26,27]. However the limited imaging depth achieved in those studies prevented visualization of complete tumor masses. This is unfortunate because the current clinical standard, provided by X-ray (Faxitron) or ultrasound, includes visualization of the complete specimen, including the whole tumor. Nevertheless, the promising results provided motivation for our study. Here we show, to our knowledge for the first time, that lipid-weighted PAT alone, combined with specialized transducers featuring exquisite bulk-tissue sensitivity, can volumetrically visualize invasive breast tumors embedded in a variety of breast tissues with similar performance to DCE-MRI but without the need for exogenous contrast agents.

1.2. Objectives

The purpose of this study was to determine the viability of a PAT-based imaging system, called **i**ntraoperative **P**hoto-**A**coustic **S**creening (iPAS), as a breast tumor assessment method by comparison of lipid-weighted iPAS tumor volume measurements to DCE-MRI, and unidimensional measurements to pathology. Also, informal comparison of iPAS imaging to ultrasonography and intraoperative X-ray imaging is presented. Finally, tumor visualization on lipid-weighted iPAS images was examined in relation to tumor grade, receptor status, and presence of *in-situ* components.

2. Materials and methods

2.1. Patient selection

Patient eligibility consisted of biopsy-confirmed invasive breast

cancer cases. Patient recruitment and study procedures were performed at a university affiliated hospital and regional breast cancer center. Seventeen consecutive patients undergoing breast conserving surgery (BCS), who also received DCE-MRI assessment as part of their diagnostic imaging studies, were asked to participate in this study with informed and signed consent in accordance with the institutional review board (IRB) of The University of Western Ontario (UWO Research Ethics Board # 105,467; LHSC Tissue Archive # 888; Lawson Approval #R-14 – 311).

2.2. iPAS system

A custom built and portable iPAS scanner was used to generate 3D image volumes through photoacoustic tomography of freshly excised and unprocessed breast lumpectomy specimens. A detailed description of the imaging system can be found elsewhere [28]. Supplementary Video 1 shows the system in operation, including the specimen handling protocol and photoacoustic scan. Fig. 1(a) and (b) illustrate a 3-D schematic representation of the front and back of the imaging system, respectively, along with all major components. Fig. 1(c) shows the system within an operating room. At the heart of the iPAS system is a 30 cm-diameter, semi-circular transducer array consisting of twenty-four 15 mm-diameter, unfocused Polyvinylidene Fluoride (PVDF) elements, with a 0.5 MHz center frequency and 120 % bandwidth. The array and an optical fiber-bundle assembly (Lumen Dynamics Group Inc., Mississauga, ON, Canada) were mounted to the effector of a 4-axis Selective Compliance Articulated Robot Arm (SCARA) robot (Epson, Model E2C351S-UL). The fiber-bundle assembly guided 30 mJ laser pulses from a Neodymium-doped Yttrium Aluminum Garnet (Nd-YAG) laser system (Phocus-Inline, Opotek Inc., CA, USA) toward the center of the transducer array, where the specimen holder restrained the sample. The maximum laser fluence at the tissue surface was 4 mJ/cm^2. The array and specimen were immersed in a large tank of water which facilitated efficient acoustic coupling. The 20 Hz pulsed laser output was selectable in the 680 nm–950 nm wavelength range. Following specimen positioning, the robot scanned the transducer array using a combination of rotational and translational motion, capturing 24,000 pressure recordings in 6 min, and covering an 11 cm × 11 cm × 3 cm volume. Specifically, to provide efficient angular coverage of the imaging volume, the 24-channel semi-circular transducer array was rotated through 10 steps of 18 degrees each. The 10 angular steps were repeated at 100 locations separated by 9 mm in the X and Y Cartesian directions, forming a square grid. The analog readings were digitized with 24 channels of a 32-channel, 14-bit, 50 MHz data acquisition system [DAQ32, MultiMagnetics, London, Canada] and transferred to a PC workstation for processing, reconstruction, and visualization. In some cases, due to concern over specimen thickness and artefacts, a scan of the opposite face was performed after revolving the specimen 180° with respect to the diagonal axis of the holder shown in Fig. 1(d).

General power to the system was provided through a hospital grade isolation transformer which also fed the laser power supply. After the iPAS scan was completed a co-registered 6.6 MHz ultrasonography system (Sonix Touch, Ultrasonix, BC, Canada) was used to scan the equivalent volume using a robotically mounted linear transducer array (L14 – 5/38, Ultrasonix, BC, Canada). To align the PA and ultrasound images, Horn's absolute orientation method was invoked [29]. To accomplish this, an agar phantom with 4 spherical graphite inclusions was used to calibrate the two (PA) and ultrasound Cartesian coordinate systems. The inclusions were visualized on both imaging instruments and their center coordinates were selected for co-registration. The ultrasound scan took 90 s to complete and acquired a total of 330 b-mode images. The photoacoustic and ultrasound scans were controlled using a PC with LabView software (National Instruments, Austin, TX, USA). Fig. 1(e) is a close up photograph of the iPAS system's water tank during an intraoperative specimen scan showing the specimen near the center, the semi-circular sensor array above, and the fiber-optic bundle below. Fig. 1(d) and (f) consist of photographs of the iPAS-compatible lumpectomy holder with 2 mutually orthogonal views showing a compressively restrained surgical specimen.

2.3. iPAS scan, volume reconstruction and processing

For the purpose of lipid-weighted imaging, an illumination wavelength of 930 nm was selected. The rationale was as follows. First, the high concentration of lipids in healthy breast tissue combined with a lipid absorption peak near 930 nm, means that the expected reduction of lipid concentration in tumors should be detectable at this wavelength [30]. Second, since the freshly excised and still metabolizing breast tissue will contain mostly deoxyhemoglobin during the iPAS scan, a more than 10 fold lower absorption due to blood compared to lipid is expected, further enhancing the overall lipid signal contribution [31,32]. Finally, since the hemoglobin distribution in the specimen may be affected by excision, it may not be a reliable indicator of malignancy. On the other hand, the lipid distribution is unaffected by excision, therefore, lipid may be a more reliable indicator of tumors.

The iPAS volumes were reconstructed using Back Projection (BP), detailed elsewhere [33]. The iPAS volumes had a resolution of approximately 2.5 mm x 2.5 mm x 2.5 mm (X Y Z), as determined previously [28]. Following BP, the volumetric results were processed through 5 iterations of K-Wave iterative image improvement using time reversal, adapted for volumetric results [34]. This procedure partially restored the amplitude of voxels by use of virtual detectors in locations where detectors were absent in the original iPAS scan, thereby mimicking the coverage of a fully enclosed signal-detection geometry.

Next, to enhance contrast prior to segmentation, the minimum (0) to maximum (255) window and level of the resulting 8-bit RGB image volumes was set to 110 – 255. Image noise reduction was carried out by use of a 2-voxel wide median filter to de-speckle and preserve sharp boundaries. Uneven illumination, caused by illumination gradients, was addressed by implementation of a pseudo-flat-field background correction available in ImageJ (1.49v, National Institutes of Health, USA). The final window and level were set by excluding very bright objects, such as black sutures, and saturating 1% of voxels so that the contrast stretching was not influenced by outliers. Image reconstruction and K-Wave correction was implemented in Matlab (MATLAB and K-wave Toolbox Release 2013a, The MathWorks, Inc., Natick, Massachusetts, United States) and image processing was carried out using ImageJ (1.49v, National Institutes of Health, USA).

2.4. Volumetric segmentation and maximum diameter measurements of iPAS results

Prior to segmentation of the tumor volumes in iPAS images, co-registered US imaging was used to confirm location of specimen edges, which were in some cases underestimated due to shadowed edge artefacts. Furthermore, specimen X-ray images obtained using a dedicated 2-D intraoperative scanner (Faxitron, Faxitron Bioptics, Tucson, Arizona, USA), were examined, and the tumor location was correlated to the tumor location in the iPAS volumes. Importantly, while specimen edges and tumor locations were correlated with US and X-ray images, tumor measurements themselves were performed using only iPAS visualization. To aid in visual referencing, image volumes from all 3-D modalities (iPAS, DCE-MRI, US) were reoriented to coincide with each other, as well as with images from the 2-D modalities (intraoperative X-ray, photography). This was done with help of surgical specimen orientation sutures, used by the surgeon to orient specimens with respect to the surgical cavity. The sutures indicated the superior aspect (short suture) and the lateral aspect (long suture)

The identified tumor masses were segmented manually by an experienced operator, who trained on images of phantoms. The segmented areas were used to measure the maximum in-slice diameter, as well as calculate the total volume based on slice thickness. The

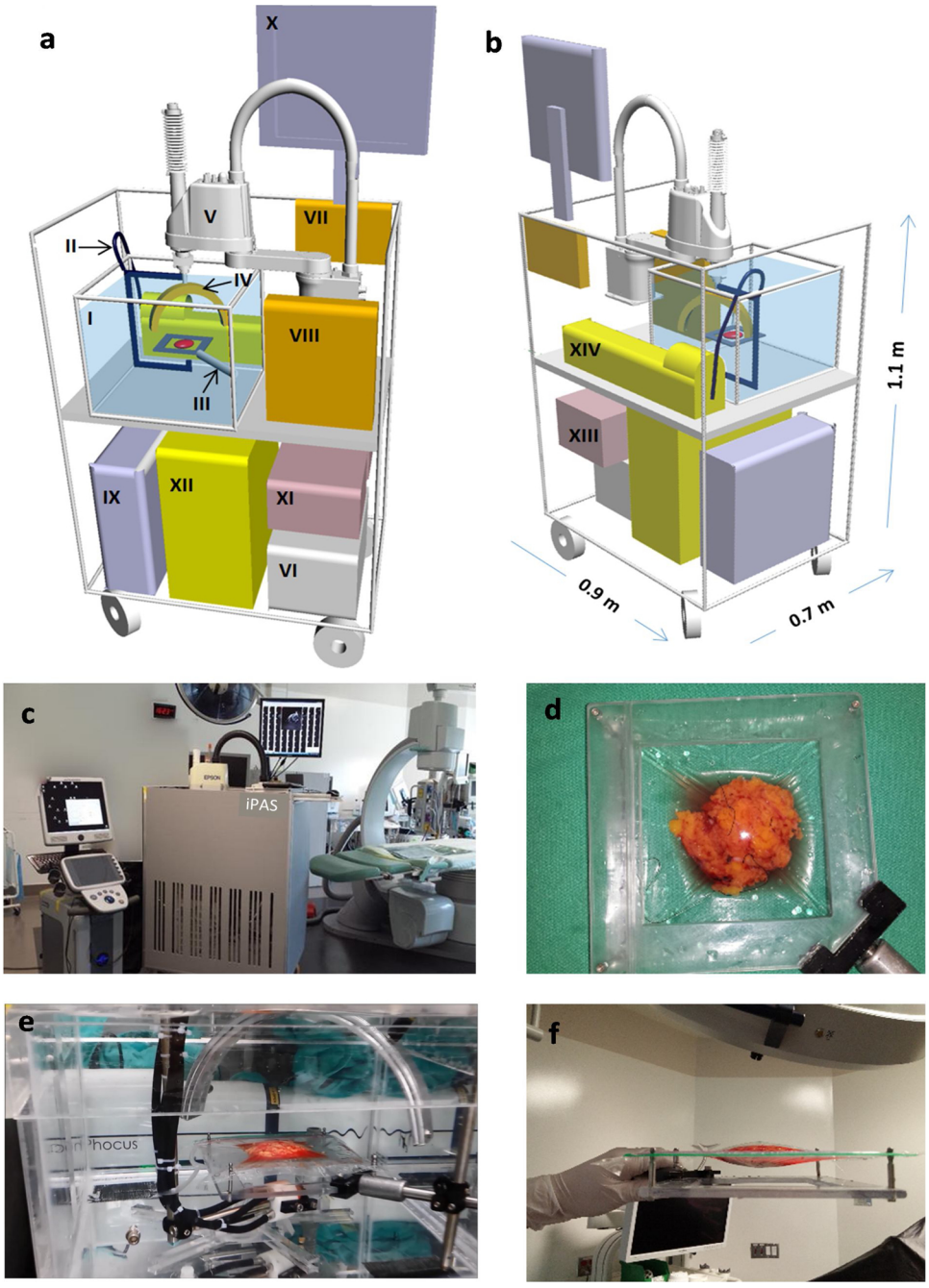

Fig. 1. (a) Three-dimensional schematic showing major components of the iPAS scanner, including water tank (**I**) which contains a fused fiber-optic bundle assembly (**II**) that is used to direct near infrared laser pulses toward the lumpectomy specimen seen restrained in the holder (**III**). Water facilitates acoustic coupling between the lumpectomy specimen and the 24-channel semi-circular sensor array (**IV**). The array and fiber-optic assembly is mounted to the effector of a 4-axis SCARA robot (Epson, Model E2C351S-UL) (**V**) which is controlled by the robot PC (**VI**). The laser induced signals detected by the transducer array are synchronized using the time delay generator [Continuum, Model TCU-1) (**VII**) and transferred to the 50 MHz data acquisition system (MultiMagnetics Inc., DAQ32) (**VIII**) where they are digitized and sent to the workstation PC (**IX**) for processing and visualization on the monitor (**X**). General power to the system is provided through a hospital grade isolation transformer (**XI**) which also feeds the laser power supply (**XII**). Fig. 1(b) depicts the back of the iPAS system including the auxiliary hospital grade uninterruptible power supply (**XIII**) and the laser system (Opotek, Phocus Inline) (**XIV**) as well as scale bars indicating the system dimensions. Fig. 1(c) is a photograph of iPAS system (center) within surgical suite as well as conventional ultrasonography system (Ultrasonix, Sonix Touch) (left). Fig. 1(d) shows a photograph of the iPAS-compatible lumpectomy holder. Fig. 1(e) is a close up photograph of the iPAS system's water tank during an intraoperative specimen scan showing the specimen near the center, the semi-circular sensor array above, and the fiber-optic bundle below. Fig. 1(f) is an orthogonal view of the specimen holder showing a compressively restrained surgical specimen.

segmentation was carried out in ImageJ. In the case of multi-focal cancer, the largest tumor was measured for unidimensional measurement and all lesions were summed for volumetric measurements.

To account for shape distortion between freshly excised specimens compressed inside the specialized iPAS tissue holder and formalin-fixed specimens at pathology, outer dimensions were compared to measurements from pathology. The findings were then compared with tumor size and shape to determine possible effect of specimen immobilization on tumor measurements.

2.5. Statistical analysis

A linear regression analysis was carried out to determine the relationship between measured quantities. Comparison of tumor maximum diameter and volume was done by calculation of Pearson's correlation coefficients, and the non-parametric Wilcoxon signed-rank test. $P = 0.05$ was considered as the significance threshold. iPAS derived volumes were compared to DCE-MRI volumes. Maximum diameters determined by iPAS were compared to DCE-MRI diameters, and separately, to pathology derived diameters. Finally, DCE-MRI diameters were also compared to diameters reported by pathology. Imaging-derived maximum diameters were measured on a single slice, and pathologic diameters were measured on a single slide. The statistical analysis was carried out using the Statistics Toolbox in Matlab (MATLAB and Statistics Toolbox Release 2013a, The MathWorks, Inc., Natick, Massachusetts, United States).

2.6. MR imaging and pathology

Gradient-echo (GE) 3D T1-weighted images were obtained in axial and sagittal planes with and without Gadovist® injection at a resolution of 0.9 mm x 0.9 mm x 1.4 mm (X Y Z). Tumors, identified by a

radiologist with extensive experience (> 10 years), were manually segmented in the axial plane based on their contrast enhancement. The segmented areas were used to calculate the total volume, as well as the maximum diameter.

Pathological examination was performed on each specimen and resulted in a breast invasive carcinoma synoptic report according to AJCC/UICC TNM 7th edition, CAP Version 3.1.0.0 (June 2012). The work was completed by, or under supervision of, a senior pathologist with more than 10 years of experience. The synoptic report was used to determine the following tumor specific information: maximum diameter, histologic type and grade, receptor status, presence of extensive intra-ductal component and presence of *in situ* disease. These properties were then compared with the photoacoustic appearance of the lesion to discover potential relationships.

3. Results

3.1. iPAS Scans and patient selection

Twelve consecutive patients were included in the iPAS study. Out of the 17 patients that agreed to participate, one patient had a DCE-MRI occult tumor due to contrast enhancement which was not significantly different from background. One patient was receiving second BCS, having had the main tumor mass removed previously. One patient had received neoadjuvant therapy and was found on pathology to be a pathologically complete responder, with no malignancy remaining. One patient presented with pure in-situ disease and no invasive tumor. And finally, one patient was found to have a radial scar lesion. The remaining 12 patients were included in the study.

The imaging scan duration was 6 min and 1.5 min for the iPAS and US scan, respectively. In cases where the specimen was scanned from two sides, the scan duration was extended by 6 min. The iPAS/US intraoperative imaging protocol did not interfere with the standard of care as maximum tissue-ischemic time prior to formalin fixation never exceeded 60 min.

Table 1 contains a tabulated summary of patient and tumor information. Patient specific information breakdown is available in Supplementary Table 1. The average age of the patients was 49.5 with a range of 33–75 and the median age was 50.

3.2. iPAS image volume reconstruction and processing

Fig. 2(a) is a photograph of a freshly excised lumpectomy specimen belonging to 53 year old patient diagnosed with a grade III invasive ductal carcinoma (IDC) tumor in the left breast. Fig. 2(b) shows initial image reconstruction results of lipid-weighted iPAS, obtained by BP. It depicts a representative slice taken from a 3D stack scanned at a wavelength of 930 nm at a depth of 7 mm below the illumination surface. The effect of applying the K-wave iterative image improvement algorithm using time reversal is shown in Fig. 2(c). Fig. 2(d) shows the impact of a 2-voxel wide median filter, pseudo-flat-field background image correction, and contrast adjustment. Finally, Fig. 2(e) shows the corresponding slice taken from a co-registered image stack acquired using ultrasonography. The total tissue thickness when compressed inside the specimen holder was 21 mm. For reference, Fig. 2(f) and (g) summarize preoperative MRI assessment of same lesion in axial view using a GE T1-weighted acquisition without fat suppression, as well as a dynamic contrast enhanced acquisition, respectively. Accordingly, the tumor appears dark while fat appears bright in iPAS, US and GE T1-weighted MRI of Fig. 2(f), while the tumor appears bright in the DCE-MRI of Fig. 2(g).

Fig. 3 demonstrates the preoperative and intraoperative breast tumor assessment and volume measurement procedure. A 46 year old patient with a biopsy-confirmed grade I IDC in upper outer right breast received a preoperative bilateral DCE-MRI scan, shown in perspective view on the left in Fig. 3(a). The right side of the figure shows color-depth encoded MRI image stacks of the indicated area. The upper stack depicts precontrast T1-weighted gradient echo MR images without fat suppression, where both the tumor mass and fibroglandular tissue apear dark while fat appears bright. Consequently this imaging mode makes it dificult to delineate the tumor mass from the surrounding fibro-glandular tissue. This difficulty is overcome using contrast enhancement as shown in the DCE-MRI slices in the lower stack on the right side of Fig. 3(a), where the tumor mass apears bright relative to the background. As a result, the tumor mass is easily identified and segmented as shown below the image stacks, where an example volume (V_{MRI}) calculation is also shown.

Fig. 3(b) shows the same assessment concept in the intraoperative setting, but this time the volume calculation is based on lipid-weighted iPAS at a wavelength of 930 nm. The left side of Fig. 3(b) shows a 3-D rendered image of the freshly excised lumpectomy along with color-depth indicated virtual slicing of the specimen. The right side shows corresponding image stacks with lipid-weighted iPAS results at the top and co-registered ultrasonography below. Consistent with the MRI assessment, iPAS tumor segmentation and volume (V_{iPAS}) calculation is also shown, where Δt_s is the MRI and iPAS slice thickness, which was set to 1 mm. Note that for purposes of simplified visualization, Fig. 3 shows slices with a 2 mm separation. Fig. 3(c), (d), and (e) show magnified images of specimen X-Ray, iPAS and US, respectively, while 3(f) depicts a photograph of the freshly excised specimen. Intriguingly, the tumor contrast in the lipid-weighted iPAS images was not diminished even though the GE T1-weighted MRI without fat subtraction clearly demonstrated that the inferior-half of the tumor bed consisted of dense fibro-glandular tissue while the superior half was embedded in fatty tissue. This finding suggested that tumor contrast in lipid-weighted iPAS was not due purely to a reduction in fat concentration associated with the malignant lesion, but instead reflected the altered lipid profile of both fatty and fibro-glandular tissue at the tumor location.

Fig. 4 is a visual summary of the imaging results for the remaining 10 lumpectomies investigated in this work. The 3D imaging results (iPAS, DCE-MRI, US) have been reoriented to approximately coincide with the intraoperative X-ray and photograph, where available. The specific slices shown here were selected due to the apparent good co-

Table 1
Patient and tumor information.

	Patient age			Tumor histologic type		Tumor histologic grade			EIC[5]	Invasive with In-situ tumor
	Mean	Median	Range	IDC[3]	ILC[4]	1	2	3		
N^1	49.5	50	33 – 75	11	1	6	4	2	2	9
%[2]				92	8	50	33	17	17	75

Numeric value.
Percent value of total number of cases.
Invasive Ductal Carcinoma.
Invasive Lobular Carcinoma.
Extensive Intraductal Component.

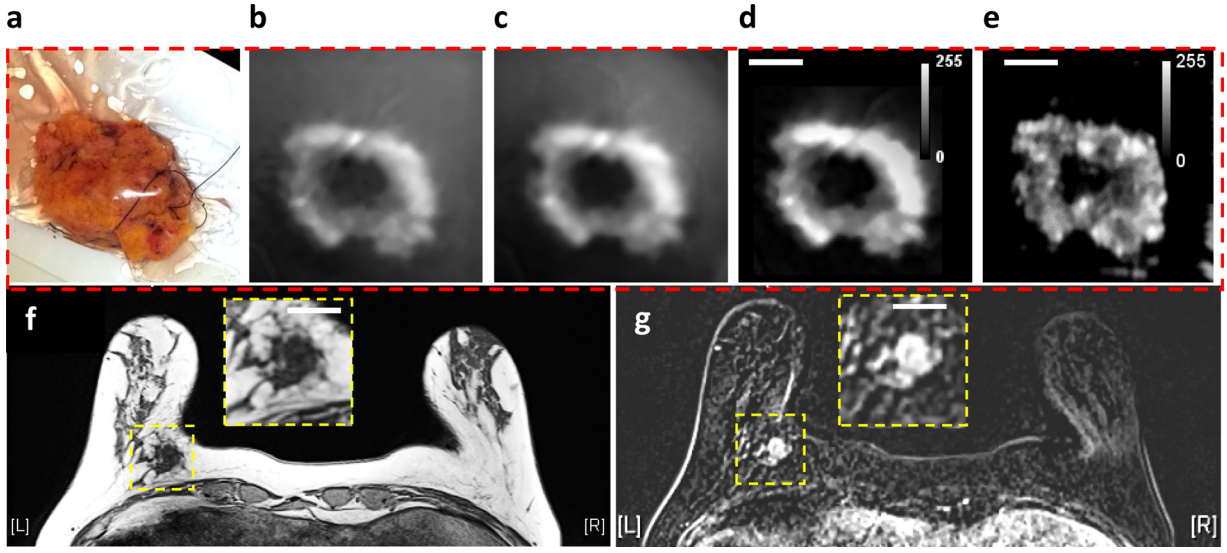

Fig. 2. (a) Photograph of freshly excised breast lumpectomy specimen belonging to 53 year old patient diagnosed with grade III invasive ductal carcinoma in the left breast. Lipid-weighted iPAS, showing compounding impact of (b) Back-projection, (c) K-wave iterative image improvement, (d) 2-voxel wide median filter and pseudo-flat-field background correction combined with contrast adjustment. (e) Co-registered US image. (f) Preoperative GE T1-weighted MRI without fat suppression in axial view showing the hypo-intense triangular-shape tumor surrounded by hyper-intense fatty tissue. (g) DCE-MRI acquisition showing same tumor as hyper-intense. The white bars represent 2 cm.

visualization of tumors in most of the imaging modalities used. The specimen thickness at iPAS/US imaging ranged from 9 mm to 22 mm, and the selected slice depth ranged from 4 mm to 9 mm below surface.

3.3. Volumetric and maximum diameter measurements

The tumor maximum diameter measurements and volumetric measurements, derived from the pathology report, DCE-MRI, and iPAS are summarized in Table 2, while Table 3 summarizes whole specimen measurements. Patient specific breakdown of the information is available in Supplementary Tables 2 and 3. For easy comparison, the Supplementary Tables list cases P1 to P12 in the same order as they appear in Figs. 2, 3 and 4. The mean tumor volume based on DCE-MRI was 1426 mm^3 (range of 94–5509 mm^3, S.D. 1759) with a median of 610 mm^3. In comparison, the mean volume from iPAS measurements was 1169 mm^3 (range of 41–4705 mm^3, S.D. 1352) and median was 757 mm^3. In terms of mean maximum tumor diameter, the measurement for pathology was 14.8 mm (range 4–39 mm, S.D. 9.3) with median 13.5 mm, DCE-MRI produced 18 mm (range 7 −43 mm, S.D. 11.7) with median 16 mm, and finally iPAS mean maximum diameter was 23.1 mm (range 9–46 mm, S.D. 11.5) with median of 23 mm.

Table 3 summarizes three orthogonal measurements of the whole lumpectomy specimens, taken from iPAS/US imaging, as well as measurements of the formalin- fixed specimens, taken from the pathology report. For comparison, the table also includes ellipsoid volumes calculated using these diameters.

3.4. Statistical analysis

The regression analysis indicated a statistically significant correlation between iPAS and DCE-MRI for volumetric tumor size ($r = 0.78$, $p = 0.003$). Moreover, the mean difference in volumetric tumor size estimated from these two modalities was not significantly different according to the Wilcoxon signed-ranked-test ($p = 0.97$), implying that the measurements were likely of the same sample population. The mean volume difference and standard deviation between iPAS and DCE-MRI were -257 ± 1093 mm^3, while the median difference was 38.6 mm^3. Compared to DCE-MRI, volume estimates by iPAS differed by a mean -3.6 ± 15 % and by a median +11 %.

Values for the remaining comparisons are summarized in Table 4 which lists the Pearson correlation coefficients and Wilcoxon signed-ranked-test results between the imaging modalities and pathology, as well as the related significance values. Table 4 also relates the mean and median volumetric size differences between DCE-MRI and iPAS as well as unidimensional size differences between DCE-MRI, iPAS and pathology. To account for the broad range of tumor sizes in this study, the sizes were compared in terms of absolute as well as relative differences.

The regression analysis resulted in four scatter plots depicting the correlation of volumetric and maximum-diameter measurements by pathology and DCE-MRI, to measurements by iPAS. Also, correlation between DCE-MRI and pathology measurements was examined. Fig. 5(a–d) shows the plots along with a line of best fit and the associated 95 % confidence intervals.

4. Discussion and future directions

4.1. Comparison of breast tumor measurements by iPAS, DCE-MRI and pathology

This investigation showed a significant and positive correlation ($r = 0.78$, $p = 0.003$) between volumetric assessment of tumors by lipid-weighted iPAS and DCE-MRI, as presented in Table 4. The non-parametric Wilcoxon signed-ranked test showed no significant difference between the two measurements ($p = 0.97$). On the other hand, unidimensional maximum diameter measurements were found to be overestimated by 5.1 ± 10.1 mm on iPAS, although still significantly positively correlated to DCE-MRI. A similar trend was seen in comparison to unidimensional pathologic measurements, where correlations were strong and positive but sizes were significantly overestimated. The average 3.2 ± 10.1 mm overestimation of tumor size on DCE-MRI compared to pathology is not unique and is well documented in literature [15,16,35]. A possible explanation for the overestimation by DCE-MRI is related to the lack of inclusion of Ductal Carcinoma In-Situ (DCIS) components as part of standard pathologic measurements of breast tumors. The problem is further compounded by difficulty in differentiating DCIS from IDC with current medical imaging technology. This pilot study did not include special instructions for pathology to perform more detailed measurements on DCIS tumor components. However, this information would have been useful because the maximum tumor diameter overestimate, found on both DCE-

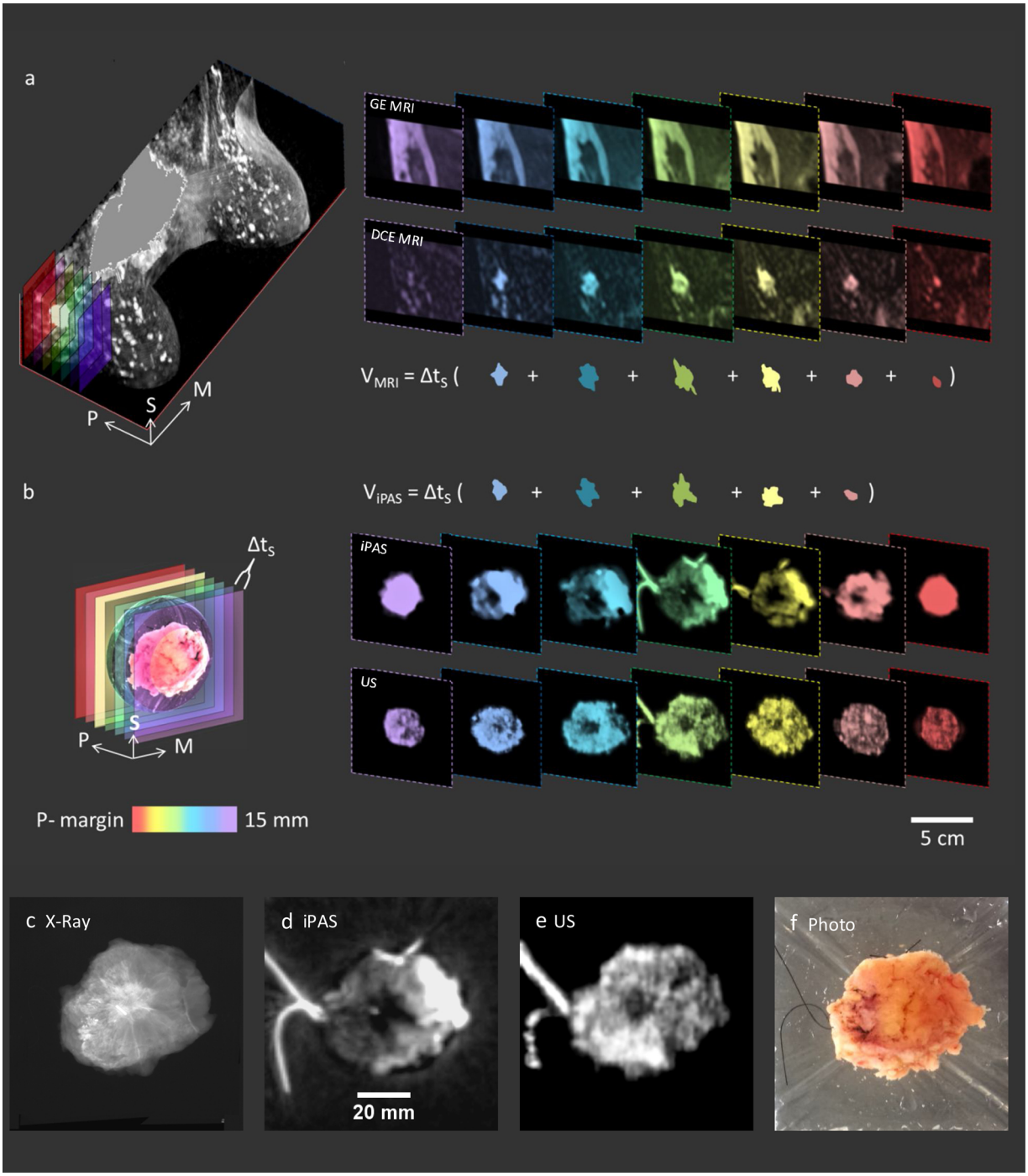

Fig. 3. Breast tumor assessment of 46 year old patient with biopsy-confirmed grade I IDC in upper outer right breast. 3(a) On the left is a bilateral DCE-MRI in perspective view, while on the right are color-depth encoded slices of indicated area in coronal view showing precontrast GE T1w MRI without fat suppression (upper stack), and contrast-enhanced slices (lower stack), as well as MRI tumor segmentation and volume (V_{MRI}) calculation. (b) Color-depth indicated virtual slicing of intraoperative specimen (left) showing corresponding slices (right) produced from iPAS (upper stack) and US (lower stack) imaging. Consistent with MRI assessment, iPAS tumor segmentation and volume (V_{iPAS}) calculation is shown, where Δt_s is the MRI and iPAS slice thickness. Orientation arrows: S-superior, M-medial, and P-posterior. Zoomed images of (c) specimen X-Ray, (d) iPAS, (e) US, and (f) photograph.

MRI and iPAS, is likely at least partially due to DCIS. Having DCIS size information would have allowed iPAS effectiveness for DCIS assessment to be estimated, and therefore, future studies focused on DCIS should ensure that detailed pathologic measurements are taken.

Tumor grade and receptor status was not found to significantly affect iPAS imaging findings or appearance. However, the two specimens found to contain extensive intra-ductal component, did appear to have many heterogeneously scattered focal hypo-intensities. This made tumor measurements somewhat difficult, compared to almost all other cases, and resulted in an above average overestimation of size by iPAS and DCE-MRI, compared to pathologic size. Nevertheless, the rather small sample size likely limited the observation of potential differences in pathological tumor features.

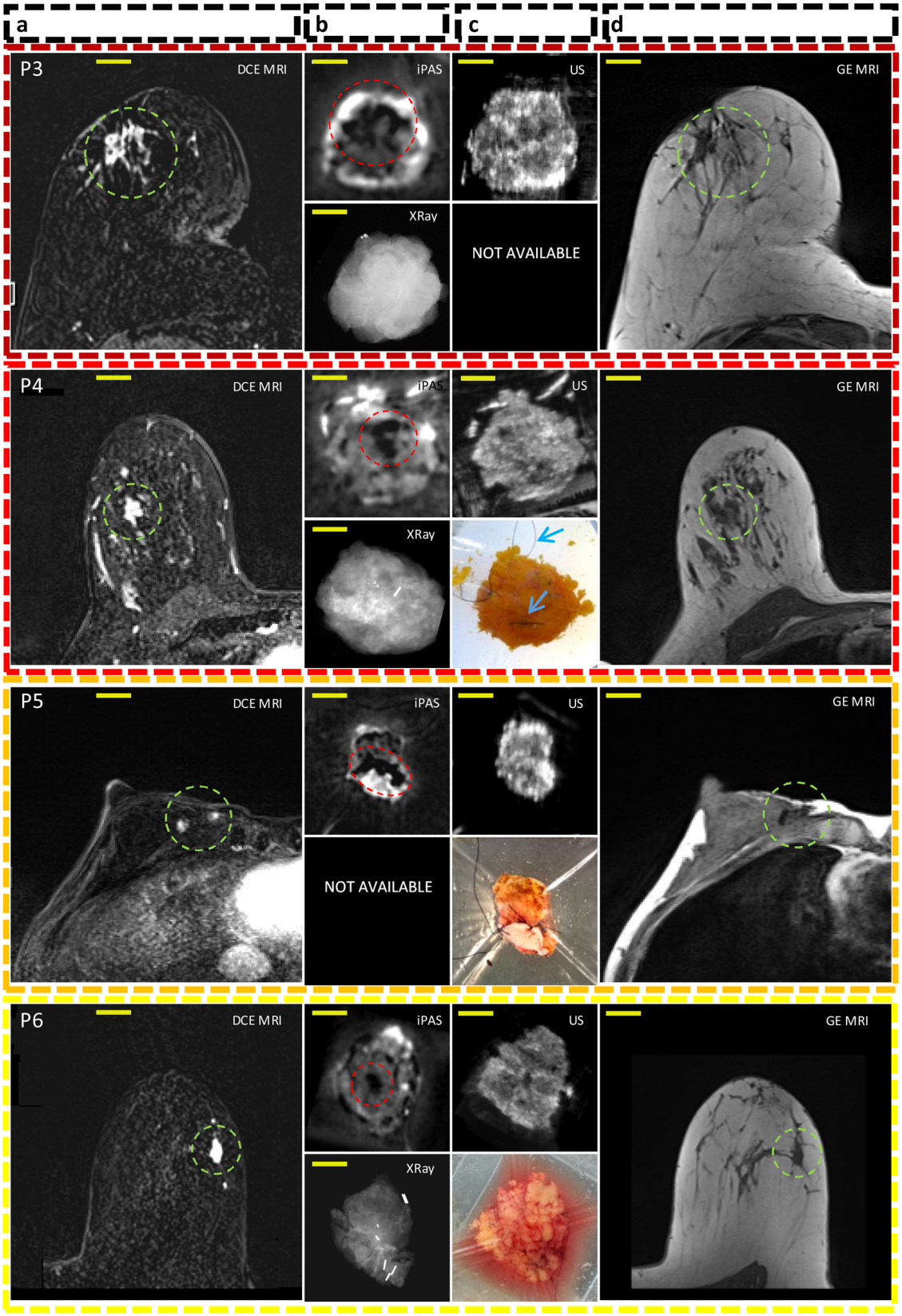

(caption on next page)

Fig. 4. Representative slices corresponding to the remaining 10 out of 12 patients diagnosed with invasive breast carcinoma acquired using DCE-MRI, lipid-weighted iPAS, US, X-RAY, photography and GE T1w MRI. Each row represents a single patient, for example, P1 for patient 1. Column (a) shows DCE-MRI in axial view of the affected breast with the relevant lesion indicated using a green circle. Column (b-top) depicts imaging results from a freshly excised lumpectomy specimen using lipid-weighted iPAS with the tumor mass outlined using a red circle. Column (b-bottom) shows the intraoperative X-RAY of same specimen. Column (c-top) displays intraoperative ultrasonography results co-registered to iPAS imaging. Column (c-bottom) shows a photograph of the specimen contained within a saline filled bag and compressively restrained by the lumpectomy holder. The photographs also demonstrate the visualization of black surgical orientation sutures attached by the surgeon to establish specimen orientation with respect to the surgical cavity and patient. For example, see blue arrows in photograph of P4. Finally, column (d) depicts the affected breast using gradient echo T1-weighted pre-contrast MRI without fat subtraction, except P10 to P12 where post-contrast (GE Post) images are shown. The tumor lesion is outlined using a green circle. The yellow bars represent 2 cm. Note: P12(a) includes a DCE-MRI insert of tumor mass in coronal view.

4.2. Effect of lumpectomy holder on measurements

While the overestimate of maximum tumor diameters by iPAS versus pathology is partially explained by the lack of inclusion of DCIS, it does not explain the average 5.1 mm overestimate of diameters on iPAS compared to DCE-MRI. However, a compelling case can be made by considering the method by which the specimen was immobilized inside the iPAS scanner. The specialized lumpectomy specimen holder that was used to restrain the samples applied significant compressive pressure on the specimens. This had the effect of flattening out the samples, making them noticeably thinner, vertically, as well as wider, horizontally. Motivated similarly to x-ray mammographic breast compression, this method of sample immobilization is well suited to iPAS because it allows greater laser fluence to reach inside the thinner compressed specimen compared to an uncompressed specimen. Unfortunately, compression may skew non-volumetric unidimensional measurement results due to specimen deformation, making maximum diameter correlations biased.

To establish a measure of specimen and tumor deformation, three orthogonal diameter measurements and associated ellipsoid volumes were calculated using pathologic as well as iPAS/US data, as shown in Table 3. Similarly to tumor maximum diameters, the resulting specimen maximum diameters were also positively correlated but significantly different. Indeed, specimen maximum diameters were overestimated by an average 9.5 ± 3.6 mm, while ellipsoid volumes were not significantly different, a trend also seen with the tumor measurements tabulated in Table 4. Therefore, a reasonable explanation is that at least part of the specimen deformation, caused by the compressive nature of the lumpectomy holder, was imparted to the lesions contained within. This finding is not entirely new as mammographic and photoacoustic compression paddles, as well as MRI breast coils, have been blamed for tumor measurement discrepancies in previous studies [5,19,36].

4.3. Participant breast density and lesion characteristics

The participants in this first-of-a-kind investigation were not representative of an average breast cancer patient population. The most common reason for MRI examination in these cases was either occult nature of tumor on US and mammography, or generally ambiguous findings due to dense breasts. This is reflected in the low mean (49.5 years) and median (50 years) age of the participants. Compared to the average age of BCS patients at our institution, the group reported here was approximately 10 years younger. For these reasons it is not surprising that the average breast density associated with the participants in this investigation was significantly higher compared to a normal population. Supplementary Table 4 includes the American College of Radiology (ACR) BI-RADS ATLAS classification of breast tissue density, encountered in this study, and the same categories have been adopted for the corresponding pathological description. The table also shows a breakdown of the DCE-MRI background parenchymal enhancement levels. While the pathological description corresponded to the limited breast tissue volume of the excised specimen, a good agreement was found with MRI, which described the entire breast. As can be seen in the table, 10 out of 12, or 83 %, of the participants had heterogeneous or extreme fibro-glandular tissue, as noted by the pathologist and radiologist. This is much higher than an average of 50 % encountered in the general female population [37]. In spite of the high breast density of the participants in this study, no reduction in tumor contrast seemed to occur, suggesting the independence of iPAS contrast and breast density. Furthermore, as Table 1 shows, 75 %, or 9 out of 12 invasive cancer cases studied contained lesions with *in-situ* components which were not included in pathologic measurements, as per current standard of care. These statistics indicate that the cases are likely more challenging than what would be expected of the general population. Therefore, interpretation of the results should be made with these differences in mind.

4.4. Image reconstruction and processing

The specificity of iPAS is owed in large part to the relative quantification of dominant tissue chromophores, extracted from deep tissue via the photoacoustic effect. Back-projection was found to be an efficient image reconstruction method to estimate the chromophore distribution inside the specimens. However, the limited aperture effect, which often plagues PAT results, likely distorted the true chromophore distribution due to the absence of sensors at key points [38,39]. We found that the K-wave image improvement method, described above, could at least partially restore voxel amplitudes in areas where intensity varied in a non-physical manner. The result was a smoother and more consistent appearance of tumors. This can be appreciated in Fig. 2 where the tumor-edge is significantly clearer in the K-wave improved image. The improved images were found to better agree with correlated x-ray and US findings, and were easier to segment. The segmentation was further aided by use of a median filter, which is often invoked in US image processing because of its ability to smooth speckle noise while preserving boundary features [40].

The benefit of K-wave iterative image improvement on the imaging results of this study indicated that detector coverage was sub-optimal. While the method was able to partially mitigate transducer detection gaps by estimating forward-model pressure measurements over a fully enclosed detection surface using time reversal, it was unable to provide any additional information. To minimize missing information caused by aperture deficits, future investigations using PAT should pay close attention to scanning geometry and transducer detection coverage.

4.5. Shadowing artefacts

Analogous to *acoustic shadowing* and *edge shadowing* artefacts in ultrasonography, sharp illumination gradients associated with iPAS imaging near sharp edges, may also cause shadowing artefacts [41]. Furthermore, areas immediately below highly optically absorbing objects, such as black surgical sutures, are effectively over-shadowed and tend to appear dark. For example, note the location of sutures in the photograph of Fig. 4(P8) and the dark band running along the top of the specimen on iPAS. These shadow-like effects can interfere with the visualization of tumors, which also present as hypo-intense volumes. In cases where the tumor was abutting the margins, or was otherwise located peripherally, this interference sometimes caused the edges of the specimen to be difficult to delineate from the tumors. We addressed this

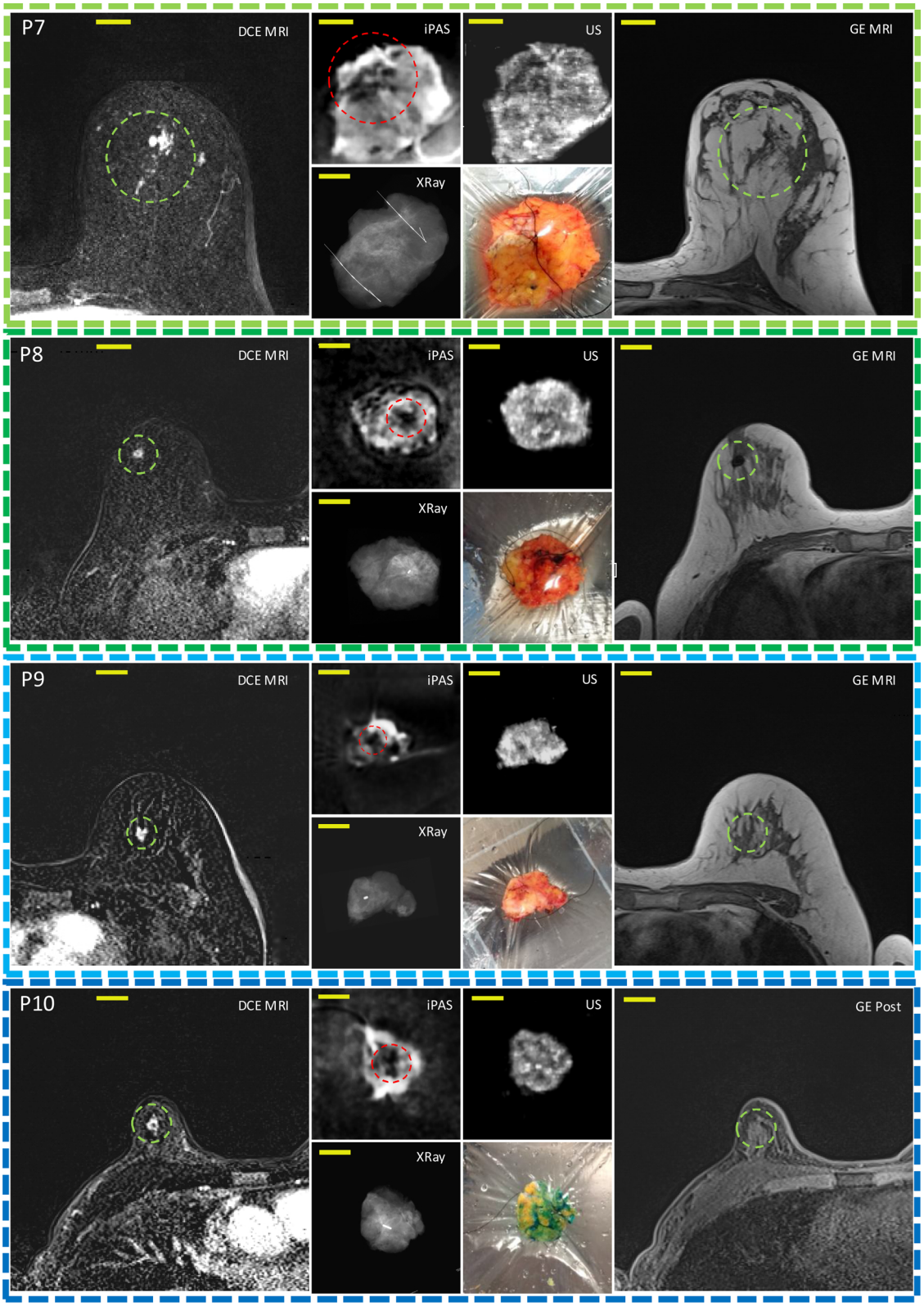

Fig. 4. (*continued*)

problem by collecting co-registered US images, allowing us to define the edges of the specimens prior to tumor segmentation. Nevertheless, improving the illumination scheme may address this problem without the reliance on ultrasonography, reducing the complexity and cost of the iPAS system.

5. Conclusion

The work presented here demonstrated a new method of visualizing whole breast tumors utilizing lipid- rather than hemoglobin-weighted PAT. This advancement was facilitated by the development of acoustic detector technology with exquisite sensitivity to signals generated by

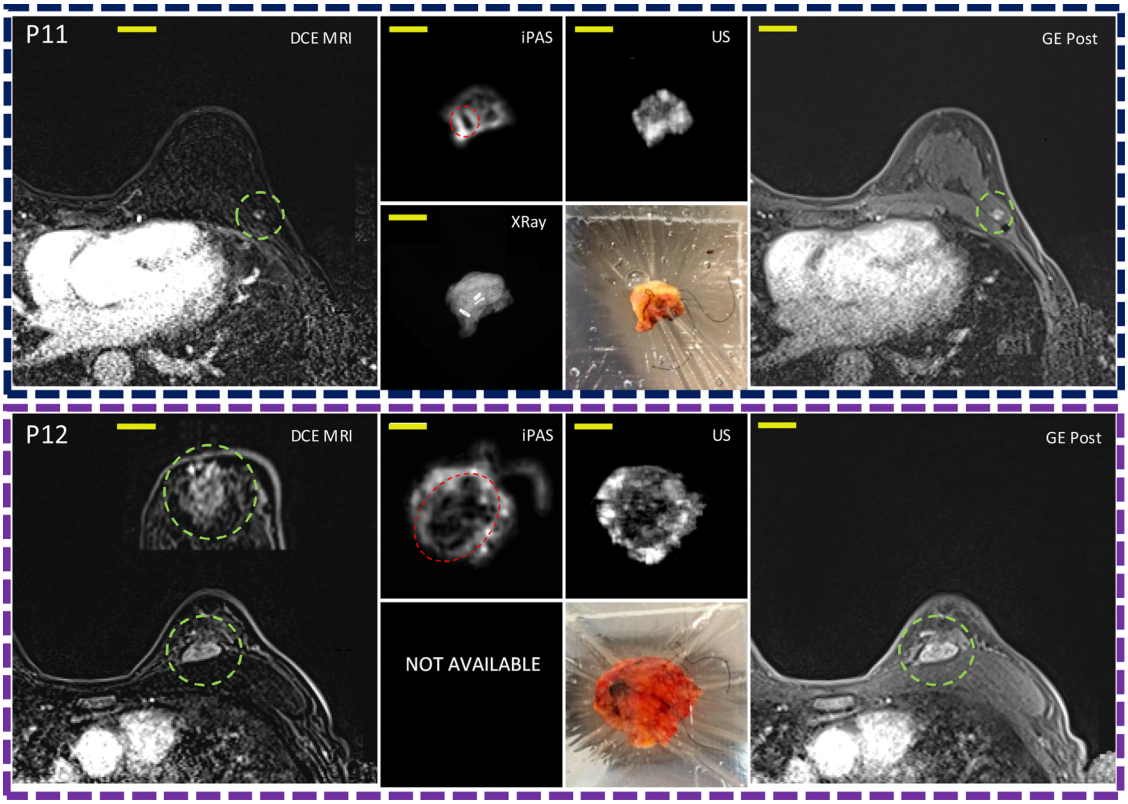

Fig. 4. (*continued*)

Table 2
Maximum tumor diameters and volumetric measurements for iPAS, DCE-MRI and pathology.

	Maximum tumor diameter (mm)			Tumor volume (mm^3)	
	Pathology	DCE-MRI	iPAS	DCE-MRI	iPAS
Mean	14.8	18	23.1	1426	1169
Median	13.5	16	23	610	757
S.D.	9.3	11.7	11.5	1759	1352

bulk tissues measuring centimeters rather than millimeters in scale. As a result, the system was able to take advantage of the high proportion of photoacoustic energy released at lower frequencies, associated with large features like tumors, rather than higher frequencies, from small features such as vasculature.

The investigation outlined a comparison of breast tumor size measured by pre-operative DCE-MRI, intra-operative iPAS, and post-operative pathology. The strong positive correlations of up to r = 0.78 that were found between iPAS and other modalities as well as pathology, provided confidence that iPAS has utility for imaging during breast surgery. We found that volumetric tumor measurements were more reliable than unidimensional measurements, echoing previous studies with established medical imaging technologies. These findings open a new window and a fresh perspective on malignancy visualization and assessment. Compelling future research directions were highlighted by brief examination of the possible influence of DCIS tumor components on iPAS tumor measurements, the importance of optimal sensor coverage, as well as the nature of shadowing artefacts in iPAS. Finally, perhaps the most impactful aspect of this investigation may be the apparent independence of iPAS tumor contrast and breast density. This finding implies that a breast imaging system based on iPAS technology may offer fast and safe high-contrast tumor visualization at low cost and without the need for contrast agents or ionizing radiation exposure. In addition to intraoperative applications highlighted here, the potential impact of this technology on breast screening programs as well as preoperative imaging is significant.

Funding source

Ivan Kosik was supported by the Translational Breast Cancer Research Unit (TBCRU) as well as The University of Western Ontario (WGRS). Research funding was provided by the Natural Sciences and Engineering Research Council (NSERC, 312232 – 2009), the Canadian Institute for Health Research (CIHR, 220,298), and the Lawson Health Research Institute (LHRI, Lawson Innovation Prize). MultiMagnetics Inc. provided support with respect to the development of the data acquisition hardware.

Table 3
Specimen diameters and corresponding ellipsoid volumes determined by pathology and iPAS.

	Specimen diameters (D) and volumes from pathology				Specimen diameters and volumes from iPAS/US imaging[a] (mm)			
	Max D (mm)	D2 (mm)	D3 (mm)	Ellipsoid Volume (cm^3)	Max D (mm)	D2 (mm)	D3 (mm)	Ellipsoid volume (cm^3)
Mean	49	44.5	25	25.4	58.5	49	14.5	21.3
Median	50	42.5	22.6	29.5	59.5	48	15	26.2
S.D.	13.6	12.3	6.8	19.4	14.1	13.2	4.7	17.3

[a] Specimen perimeter was outlined using iPAS images unless artefacts obscured edge, in which case US was used.

Table 4
Correlation coefficients and statistical assessment between the imaging modalities for tumor size and whole specimen size.

Comparison pairs	Pearson correlation R-value	Wilcoxon signed rank test	Mean difference (S.D.)		Median difference	
			(dimension)	(%)	(dimension)	(%)
iPAS vs DCE-MRI tumor volumes	0.78 (p = 0.003)	p = 0.97	−257 (1093) mm^3	3.6 (15)	38.6 mm^3	11
iPAS vs DCE-MRI tumor max diameter	0.54 (p = 0.07)	p = 0.064	5.1 (11.1) mm	28 (61)	4.5 mm	28
iPAS vs pathology tumor max diameter	0.87 (p = 0.0002)	p = 0.0015[a]	8.3 (5.61) mm	46 (31)	8.5 mm	47
DCE-MRI vs pathology tumor max diameter	0.56 (p = 0.06)	p = 0.55	3.2 (10.1) mm	17 (54)	0 mm	0
iPAS vs pathology specimen max diameter	0.97 (p < 0.0001)	p = 0.00049[a]	9.5 (3.61) mm	18 (6.8)	10 mm	19
iPAS vs pathology specimen ellips. volume	0.98 (p < 0.0001)	p = 0.052	−3.29 (4.54) cm^3	14 (19)	−2.43 cm^3	10

[a] Indicates significant difference.

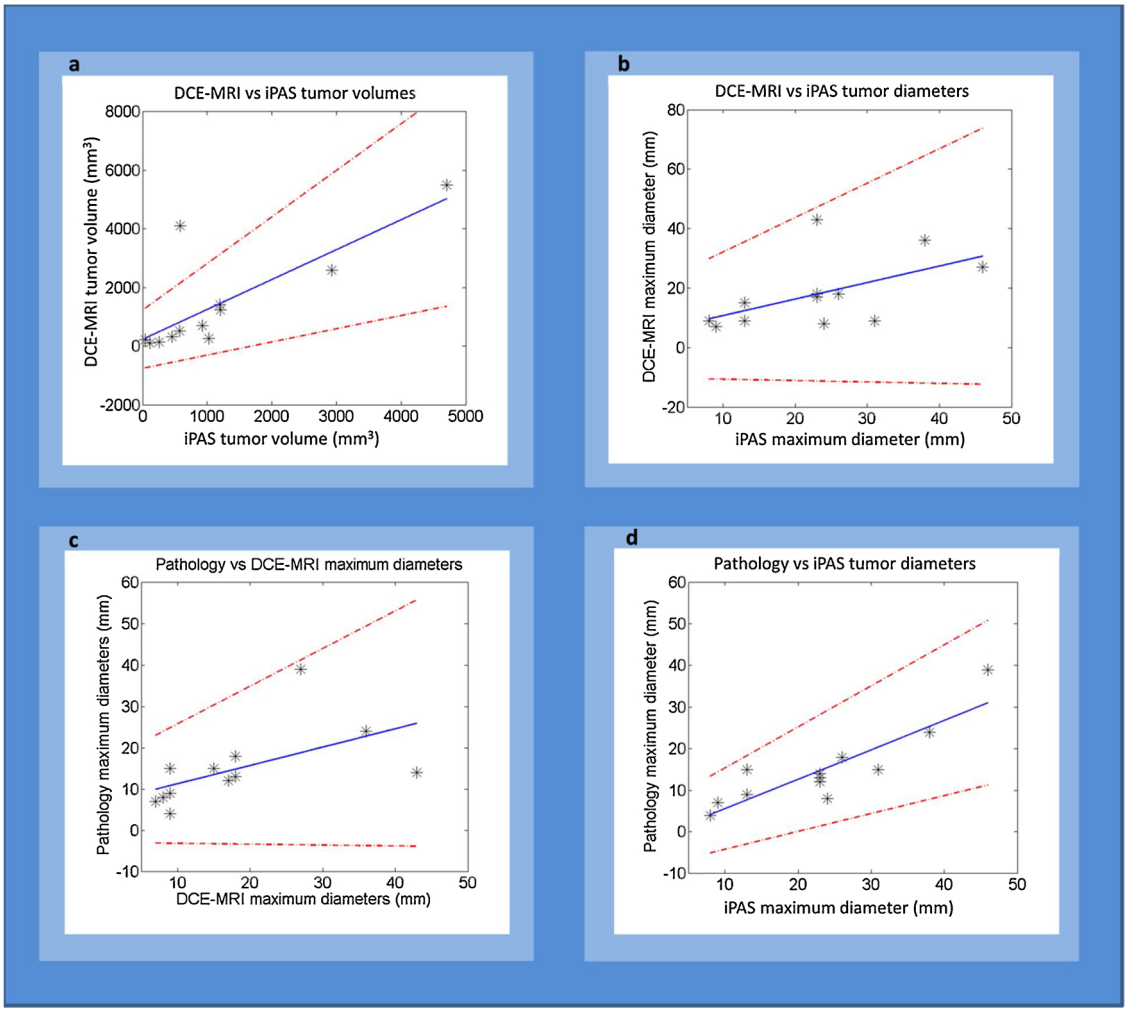

Fig. 5. Regression analysis and scatter plots with line of best fit (blue) and 95 % confidence intervals (red dashed) for comparing volumes (a) and maximum diameters (b, c and d) measured by iPAS, pathology and DCE-MRI.

The study sponsors had no involvement in its design, writing, interpretation or publication.

Use of human subjects

All studies were carried out with signed informed consent and the approval of the institutional review board of The University of Western Ontario (UWO Research Ethics Board # 105,467; LHSC Tissue Archive # 888; Lawson Approval #R-14−311).

Declaration of Competing Interest

The authors have no relevant financial interests in the manuscript and no other potential conflicts of interest to disclose.

Acknowledgements

Ivan Kosik was supported by the Translational Breast Cancer Research Unit (TBCRU) as well as The University of Western Ontario (WGRS). Research funding was provided by the Natural Sciences and

Engineering Research Council (NSERC, 312232-2009), the Canadian Institute for Health Research (CIHR, 220298), and the Lawson Health Research Institute (LHRI, Lawson Innovation Prize). MultiMagnetics Inc. provided support with respect to the development of the data acquisition hardware. The authors thank Lynn Keenliside of Lawson Health Research Institute for technical support.

Appendix A. Supplementary data

Supplementary material related to this article can be found, in the online version, at doi:https://doi.org/10.1016/j.pacs.2020.100165.

References

[1] R.L. Siegel, K.D. Miller, A. Jemal, Cancer Statistics, 2015, CA Cancer J. Clin. 65 (1) (2015) 5–29, https://doi.org/10.3322/caac.21254.
[2] M.J. Yaffe, A.K. Bloomquist, D.M. Hunter, et al., Comparative performance of modern digital mammography systems in a large breast screening program Comparative performance of modern digital mammography systems in a large breast screening program, Med. Phys. 40 (112) (2013) 121915, , https://doi.org/10.1118/1.4829516.
[3] C. Balleyguier, S. Ayadi, K. Van Nguyen, D. Vanel, C. Dromain, R. Sigal, BIRADS??? classification in mammography, Eur. J. Radiol. 61 (2) (2007) 192–194, https://doi.org/10.1016/j.ejrad.2006.08.033.
[4] A.A. Tardivon, A. Athanasiou, F. Thibault, C. El Khoury, Breast imaging and reporting data system (BIRADS): magnetic resonance imaging, Eur. J. Radiol. 61 (2) (2007) 212–215, https://doi.org/10.1016/j.ejrad.2006.08.036.
[5] W.T. Yang, W.W.M. Lam, H. Cheung, M. Suen, W.W.K. King, C. Metreweli, Sonographic, magnetic resonance imaging, and mammographic assessments of preoperative size of breast cancer, J. Ultrasound Med. 16 (12) (1997) 791–797 http://www.scopus.com/inward/record.url?eid=2-s2.0-0000202613&partnerID=tZOtx3y1.
[6] P. Ananthakrishnan, F.L. Balci, J.P. Crowe, Optimizing surgical margins in breast conservation, Int. J. Surg. Oncol. 2012 (2012), https://doi.org/10.1155/2012/585670.
[7] A.C. Hargreaves, M. Mohamed, Intra-operative guidance : methods for achieving negative margins in breast conserving surgery, J. Surg. Oncol. 110 (1) (2014) 21–25, https://doi.org/10.1002/jso.23645.
[8] Y.-L. Gu, S.-M. Pan, J. Ren, Z.-X. Yang, G.-Q. Jiang, Role of magnetic resonance imaging in detection of pathologic complete remission in breast Cancer patients treated with neoadjuvant chemotherapy: a meta-analysis, Clin. Breast Cancer (2017), https://doi.org/10.1016/j.clbc.2016.12.010.
[9] D. Groheux, A. Cochet, O. Humbert, J.-L. Alberini, E. Hindié, D. Mankoff, 18F-FDG PET/CT for staging and restaging of breast Cancer, J. Nucl. Med. 57 (Suppl 1) (2016) 17S–26S, https://doi.org/10.2967/jnumed.115.157859.
[10] E.A. Eisenhauer, P. Therasse, J. Bogaerts, et al., New response evaluation criteria in solid tumours: revised RECIST guideline (version 1.1), Eur. J. Cancer 45 (2) (2009) 228–247, https://doi.org/10.1016/j.ejca.2008.10.026.
[11] J.F. Waljee, E.S. Hu, L.A. Newman, A.K. Alderman, Predictors of Re-excision among women undergoing breast-conserving surgery for Cancer, Ann. Surg. Oncol. 15 (5) (2008) 1297–1303, https://doi.org/10.1245/s10434-007-9777-x.
[12] A.M. Bosch, A.G.H. Kessels, G.L. Beets, et al., Preoperative estimation of the pathological breast tumour size by physical examination, mammography and ultrasound: a prospective study on 105 invasive tumours, Eur. J. Radiol. 48 (3) (2003) 285–292, https://doi.org/10.1016/S0720-048X(03)00081-0.
[13] L. Weir, D. Worsley, V. Bernstein, The value of FDG positron emission tomography in the management of patients with breast cancer, Breast J. 11 (3) (2005) 204–209 doi:TBJ21625[pii]\r10.1111/j.1075-122X.2005.21625.x.
[14] B. Schaefgen, M. Mati, H.P. Sinn, et al., Can Routine Imaging After Neoadjuvant Chemotherapy in Breast Cancer Predict Pathologic Complete Response? Ann. Surg. Oncol. 23 (3) (2015) 789–795, https://doi.org/10.1245/s10434-015-4918-0.
[15] I.V. Gruber, M. Rueckert, K.O. Kagan, et al., Measurement of tumour size with mammography, sonography and magnetic resonance imaging as compared to histological tumour size in primary breast cancer, BMC Cancer 13 (June 2005) (2013) 328, https://doi.org/10.1186/1471-2407-13-328.
[16] G.L. Menezes, F.M. Knuttel, B.L. Stehouwer, R.M. Pijnappel, M.A. van den Bosch, Magnetic resonance imaging in breast cancer: a literature review and future perspectives, World J. Clin. Oncol. 5 (2) (2014) 61–70, https://doi.org/10.5306/wjco.v5.i2.61.
[17] S. Manohar, S.E. Vaartjes, J.C.G. van Hespen, et al., Initial results of in vivo non-invasive cancer imaging in the human breast using near-infrared photoacoustics, Opt. Express 15 (19) (2007) 12277–12285, https://doi.org/10.1364/OE.15.012277.
[18] R.A. Kruger, C.M. Kuzmiak, R.B. Lam, et al., Dedicated 3D photoacoustic breast imaging dedicated 3D photoacoustic breast imaging, Med. Phys. 40 (11) (2013) 113301, https://doi.org/10.1118/1.4824317.
[19] M. Heijblom, D. Piras, F.M. van den Engh, et al., The state of the art in breast imaging using the Twente Photoacoustic Mammoscope: results from 31 measurements on malignancies, Eur. Radiol. 26 (11) (2016) 3874–3887, https://doi.org/10.1007/s00330-016-4240-7.
[20] Sa. Ermilov, T. Khamapirad, A. Conjusteau, et al., Laser optoacoustic imaging system for detection of breast cancer, J. Biomed. Opt. 14 (2) (2009) 24007, https://doi.org/10.1117/1.3086616.
[21] A. Binte, E. Attia, S. Yee, et al., Photoacoustics Noninvasive real-time characterization of non-melanoma skin cancers with handheld optoacoustic probes, Biochem. Pharmacol. 7 (2017) 20–26, https://doi.org/10.1016/j.pacs.2017.05.003.
[22] L.V. Wang, S. Hu, Photoacoustic tomography : in vivo imaging from organelles to organs, Science 335 (80 March) (2012) 1458–1462.
[23] V.S. Dogra, B.K. Chinni, K.S. Valluru, J.V.M. Joseph, Ultispectral photoacoustic imaging of prostate Cancer : preliminary ex - vivo results, J. Clin. Imaging Sci. 3 (3) (2015) 1–7, https://doi.org/10.4103/2156-7514.119139.
[24] I. Kosik, Program I. Carson JJL, L. Health, S. Joseph, Combined 3D photoacoustic and 2D fluorescence imaging of indocyanine green contrast agent flow, Proc. SPIE. Int. Soc. Opt. Eng. 8581 (2013) 1–8, https://doi.org/10.1117/12.2005269.
[25] M.B. Roumeliotis, I. Kosik, J.J.L. Carson, 3D photoacoustic imaging using starting, Sparse array with 60 transducers. 8223 (2012), https://doi.org/10.1117/12.908841 82233F-82233F-6.
[26] Y. Goh, G. Balasundaram, et al., Multispectral Optoacoustic Tomography in Assessment of Breast Tumor Margins During Breast-Conserving Surgery: A First-in-human Case Study, Clin. Breast Cancer 18 (6) (2018) e1247–e1250, https://doi.org/10.1016/j.clbc.2018.07.026.
[27] L. Xi, S.R. Grobmyer, L. Wu, et al., Evaluation of breast tumor margins in vivo with intraoperative photoacoustic imaging, Opt. Express 20 (8) (2012) 8726–8731.
[28] I. Kosik, A. Chamson-reig, P. Wong, et al., Intraoperative photoacoustic screening of breast cancer : a new perspective on malignancy visualization and surgical guidance cancer, J. Bioimed. Opt. 24 (5) (2019), https://doi.org/10.1117/1.
[29] B.K.P. Horn, Closed-form solution of absolute orientation using unit quaternions, J. Opt. Soc. Am. A 4 (4) (1987) 629, https://doi.org/10.1364/JOSAA.4.000629.
[30] P.G. Anderson, J.M. Kainerstorfer, A. Sassaroli, et al., Broadband optical mammography: chromophore concentration and hemoglobin saturation contrast in breast cancer, PLoS One 10 (3) (2015) 1–23, https://doi.org/10.1371/journal.pone.0117322.
[31] P. Taroni, A.M. Paganoni, F. Ieva, et al., Non-invasive optical estimate of tissue composition to differentiate malignant from benign breast lesions : a pilot study, Sci. Rep. 7 (40683) (2017) 1–11, https://doi.org/10.1038/srep40683.
[32] S. Konugolu, V. Sekar, A.D. Mora, Diffuse optical characterization of collagen absorption from 500 to 1700 nm, J. Biomed. Opt. 22 (1) (2017) 015006, https://doi.org/10.1117/1.JBO.22.1.015006.
[33] M. Xu, L.V. Wang, Universal back-projection algorithm for photoacoustic computed tomography, Phys. Rev. E 71 (1) (2005) 16706, https://doi.org/10.1103/PhysRevE.71.016706.
[34] B. Treeby, B. Cox, Iterative Image Improvement Using Time Reversal, (2016) Published http://www.k-wave.org/documentation/example_pr_2D_tr_iterative.php.
[35] H.-W. Lai, D.-R. Chen, Y.-C. Wu, et al., Comparison of the diagnostic accuracy of magnetic resonance imaging with sonography in the prediction of breast Cancer tumor size: a concordance analysis with histopathologically determined tumor size, Ann. Surg. Oncol. 22 (2015) 3816–3823, https://doi.org/10.1245/s10434-015-4424-4.
[36] R.H. El Khouli, K.J. Macura, I.R. Kamel, Bluemke D a, Jacobs M a, The effects of applying breast compression in dynamic contrast material-enhanced MR imaging, Radiology 272 (1) (2014) 79–90, https://doi.org/10.1148/radiol.14131384.
[37] Radiology Ac of. Breast Density Breast cancer screening. https://www.acr.org/~/media/ACR/Documents/PDF/QualitySafety/Resources/Breast-Imaging/Breast-Density-bro_ACR_SBI_lores.pdf.
[38] L. Yao, H. Jiang, Photoacoustic image reconstruction from few-detector and limited-angle data, Biomed. Opt. Express 2 (9) (2011) 2649, https://doi.org/10.1364/BOE.2.002649.
[39] G. Paltauf, R. Nuster, P. Burgholzer, Weight factors for limited angle photoacoustic tomography. 54 (11) (2011) 3303–3314, https://doi.org/10.1088/0031-9155/54/11/002.Weight.
[40] Shibin Wu, Qingsong Zhu, Yaoqin Xie, Evaluation of various speckle reduction filters on medical ultrasound images, 2013 35th Annu Int Conf IEEE Eng Med Biol Soc (2013) 1148–1151, https://doi.org/10.1109/EMBC.2013.6609709.
[41] M.K. Feldman, S. Katyal, M.S. Blackwood, US artifacts, Radiographics 29 (4) (2009) 1179–1189, https://doi.org/10.1148/rg.294085199.

Ivan Kosik received his PhD in medical biophysics from the Western University, London, Ontario, Canada, in 2018. He received his honors BSc degree in physics from Western University with a specialization in medical physics. Currently, he is a research member of the Lawson Health Research Institute at St. Joseph's Hospital in London, Ontario. He is also the founder and director of Superior Assembly Inc., a custom assembly services company.

Dr. Muriel Brackstone attended Western University, where she received a Master's degree in Neurosciences in 1994. She attended Medical School at UWO and graduated in 1999 (Gold Medallist). She received her training in General Surgery at Western Ontario and became a Fellow of the Royal College of Surgeons in 2004. She completed a Master's Degree in Clinical Epidemiology and Biostatistics from Western University in 2008 followed by a PhD in Pathology (Clinical Trials) from Western University from 2009-2014.

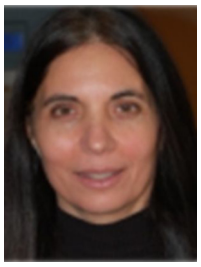

Dr. Anat Kornecki is an Associate Professor of Medical Imaging, Head of the Division of Breast Imaging at the Western University and Regional Breast Imaging Lead at the South West Regional Cancer Program. Her main area of research is breast imaging.

Astrid Chamson-Reig is a Research Coordinator with the Imaging program at the Lawson Health Research Institute in London, Ontario, Canada. She provides support to the research of Dr. Jeffrey Carson in Optics and Photoacoustic Imaging, conducting the clinical studies and mentoring students in the lab. She is responsible for website management and member support for The Bioelectromagnetics Society, and the online abstract submission system, preparation of conference Program and Abstract Proceedings for BioEM Annual meetings.

Philip Wong received his MSc in Medical Biophysics from Western University in 2014. His main area of research was photoacoustic tomography with a focus on system design optimization.

Dr. Jeffrey Carson is a scientist at the Lawson Health Research Institute and Associate Professor at the University of Western Ontario. He is an expert on optical imaging systems. His laboratory specializes in optical device development and led early developments on snapshot 3D photoacoustic tomography, snapshot multispectral imaging, and photonic devices for optical imaging and sensing. His experience includes managing large R&D projects, raising funds for research and commercialization activities. In 2015, he co-founded Spectral Devices Inc. to commercialize pixelated multispectral filter array technology developed in his laboratory.